

A comparative study of deconvolution techniques for quantum-gas microscope images

A. La Rooij^a, C. Ulm, E. Haller, S. Kuhr

University of Strathclyde, Department of Physics, SUPA, Glasgow G4 0NG, United Kingdom

(Dated: July 19, 2022)

Quantum-gas microscopes are used to study ultracold atoms in optical lattices at the single-particle level. In these system atoms are localised on lattice sites with separations close to or below the diffraction limit. To determine the lattice occupation with high fidelity, a deconvolution of the images is often required. We compare three different techniques, a local iterative deconvolution algorithm, Wiener deconvolution and the Lucy-Richardson algorithm, using simulated microscope images. We investigate how the reconstruction fidelity scales with varying signal-to-noise ratio, lattice filling fraction, varying fluorescence levels per atom, and imaging resolution. The results of this study identify the limits of single-atom detection and provide quantitative fidelities which are applicable for different atomic species and quantum-gas microscope setups.

I. INTRODUCTION

Quantum-gas microscopes have revolutionized the study of ultracold atoms in optical lattices by allowing the simulation and observation of many-body quantum systems at the single-atom level [1, 2]. In recent years, researchers have been able to experimentally observe strongly correlated quantum phases, such as bosonic and fermionic Mott insulators [3–7], anti-ferromagnetic phases [8, 9] and use ultracold gases to probe complex quantum dynamics [2, 10–13] using direct fluorescence imaging of ultracold atoms.

Many recent quantum-gas experiments use different atomic species in various lattice geometries [14–18]. In all these experiments, atoms are detected via fluorescence imaging, with a resolution close to the diffraction limit, which is on the order of the lattice spacing of about 500 nm [19–22]. A high fidelity of the atom detection is essential for quantum simulation and quantum computation experiments. However, determining the presence or absence of an atom on a lattice site can be challenging in very dense atomic clouds, such as atoms in a Mott-insulating state with near unit filling, in which single empty lattice sites need to be identified with high fidelity [11]. In order to achieve this, the fluorescence images are usually processed using deconvolution techniques, such as the Lucy-Richardson method [23, 24], the Wiener deconvolution [25] and a local iterative (LR) deconvolution algorithm [3]. Which of these techniques is used varies throughout the community, and it is not a priori known which one achieves the highest atom detection fidelity in a specific experimental scenario.

Here we present a systematic study of these three deconvolution methods and characterise their performance as a function of lattice filling and signal-to-noise ratio (SNR) of the images and specific details of the imaging system, such as the magnification and pixelation. To study the effects of these parameters systematically, we created simulated images with a known atom occupancy that match experimental images.

This article is structured as follows. In Section II it is shown how we simulate realistic single-atom-resolved fluorescence images from a known atomic distribution on a square lattice, including a realistic noise model. In Section III we introduce the three deconvolution techniques used in this study. The results are presented in Section IV where we first compare the different techniques using a uniform fluorescence signal from the atoms, then it is shown how the detection fidelity is affected by a varying fluorescence signal amplitude. In the last Section we vary imaging resolution, magnification and camera pixel sizes to study how much signal is required to obtain an optimal reconstruction.

II. SIMULATION OF FLUORESCENCE IMAGES

In typical quantum-gas microscope experiments, atoms are detected in a two-dimensional optical lattice via fluorescence imaging by a high-numerical-aperture microscope objective. Localised on individual lattice sites, the fluorescing atoms can be approximated as ideal point sources. Depending on the numerical aperture NA of the objective and the wavelength of the fluorescence light, λ , the image of a point source is given by the point-spread function

$$\text{PSF}[\tilde{r}(x, y)] = \left[\frac{2J_1(\tilde{r})}{\tilde{r}} \right]^2, \text{ with } \tilde{r}(x, y) = \frac{2\pi\text{NA}}{\lambda} \sqrt{x^2 + y^2}, \quad (1)$$

^a arthur.larooij@strath.ac.uk

where x and y are the coordinates in the object plane and $J_1(r)$ is the Bessel function of the first kind. The Rayleigh criterion states that in order to distinguish two point sources, the central intensity peak of one source must lie outwith the first minimum of the other, which is at $d_{\min} = 0.61\lambda/\text{NA}$. In an optical lattice of wavelength λ_1 , atoms in neighbouring lattice sites are separated by $a = \lambda_1/2$, which is often of similar size compared to the diffraction limit d_{\min} . As a result, it is challenging to resolve the atoms or to determine the presence of individual defects in densely filled optical lattices, as it is the case, e.g., for atoms in a Mott-insulating state [3, 4].

It is the scope of this article to determine how accurately we can detect atoms in a fluorescence image as a function of signal-to-noise ratio, varying fluorescence levels, and of imaging resolution. To study the effects of these parameters systematically, we create simulated images with a known atom occupancy, which we then retrieve using one of the deconvolution techniques mentioned above, giving access to a quantitative measure of the reconstruction fidelity. In an experimental realisation, a high-NA objective collects atomic fluorescence light, which is imaged onto a electron-multiplying CCD (EMCCD) camera. Noise in the images arises from background counts and from the electron-multiplying amplification process, which we both include in our simulations. In the following we describe step by step how our simulated images are created.

1. We start with a known binary occupation of atoms on the lattice, $n_{k,l} = 0$ or 1, on a two-dimensional square array with $N^2 \approx 100 \times 100$ lattice sites with indices k and l . The binary occupation reflects the fact that in most quantum-gas microscope setups, pairs of atoms on the same lattice site undergo light-assisted inelastic collisions and are lost before they emit any significant amount of fluorescence [1, 3]. We define as the filling factor, η , the fraction of lattice sites containing one atom. The simulated images contain a central region of interest with N^2 lattice sites which are randomly populated with filling factors $10\% < \eta < 90\%$.
2. The lattice occupation $n_{k,l}$ is multiplied with the the number of photon counts per atom, $A_{k,l}$. In the first part of our study we keep $A_{k,i}$ constant, and later simulate atoms with varying photon counts with mean \bar{A} and variance ΔA .
3. The lattice occupation $n_{k,l}$ is convolved with the point-spread function $\text{PSF}(\tilde{r})$ of eq. 1, yielding the intensity distribution $O(x, y)$ in the object plane:

$$O(x, y) = \sum_{k=0}^{N-1} \sum_{l=0}^{N-1} n_{k,l} A_{k,l} \text{PSF}[\tilde{r}(x - ka, y - la)]. \quad (2)$$

4. To obtain a simulated CCD camera image with image magnification M , the function $O(x/M, y/M)$ is discretized in steps of the camera pixel size d_{pix} (typically $5\text{-}20 \mu\text{m}$). This yields the image as 512×512 matrix with values $I_{i,j}$.
5. A random background signal $\Gamma_{\text{BG}}(i, j)$ is added to each pixel of the simulated camera image. This background signal is dominated by stray photons from lasers used in the cooling and trapping process, and it can vary significantly between experiments. The random values $\Gamma_{\text{BG}}(i, j)$ have a half-normal probability distribution $P_{\text{BG}}(\mu, \sigma_{\text{BG}})$, with offset μ and width σ_{BG} :

$$P_{\text{HN}}(n|\mu, \sigma) = \sqrt{\frac{2}{\pi}} \frac{1}{\sigma_{\text{BG}}} \exp \left[-0.5 \left(\frac{n - \mu}{\sigma_{\text{BG}}} \right)^2 \right]. \quad (3)$$

In our simulation we fix $\mu = 200$ to match the offset count rate of our Andor Ixon DU-897 camera. This noise model accurately simulates our experimental images [26]. Using the average photon count \bar{A} from step (ii) and σ_{BG} we define the signal-to-noise ratio (SNR) of our simulated images as $\text{SNR} = \bar{A}/\sigma_{\text{BG}}$.

6. The amplification process of the EMCCD camera as well as the discretisation of the image due to the camera's pixel size introduce noise. These noise sources have been compared and quantified in a recent study [27] which we use as a basis for our simulation. In our case, a Poissonian filter is applied to simulate the signal amplification process of the EMCCD camera [28, 29], and the effect of the pixel size is discussed at the end of Section IVc.

Fig. 1 illustrates the various steps involved in the simulations process. For the simulations in Sections IVa-b we have chosen $\lambda = 770.1 \text{ nm}$, $\text{NA} = 0.69$, $a = 532 \text{ nm}$, $M = 72$, pixel size $d_{\text{pix}} = 13 \mu\text{m}$ which gives $d_{\min} = 691 \text{ nm}$, matching the parameters used for fluorescence imaging of ultracold ^{40}K atoms in a square lattice ($\lambda_1 = 1064 \text{ nm}$) [26]. For these parameters, the atoms are spaced at $a = \lambda_1/2$ and cannot be considered resolved using the Rayleigh criterion ($a = 0.88 d_{\min}$).

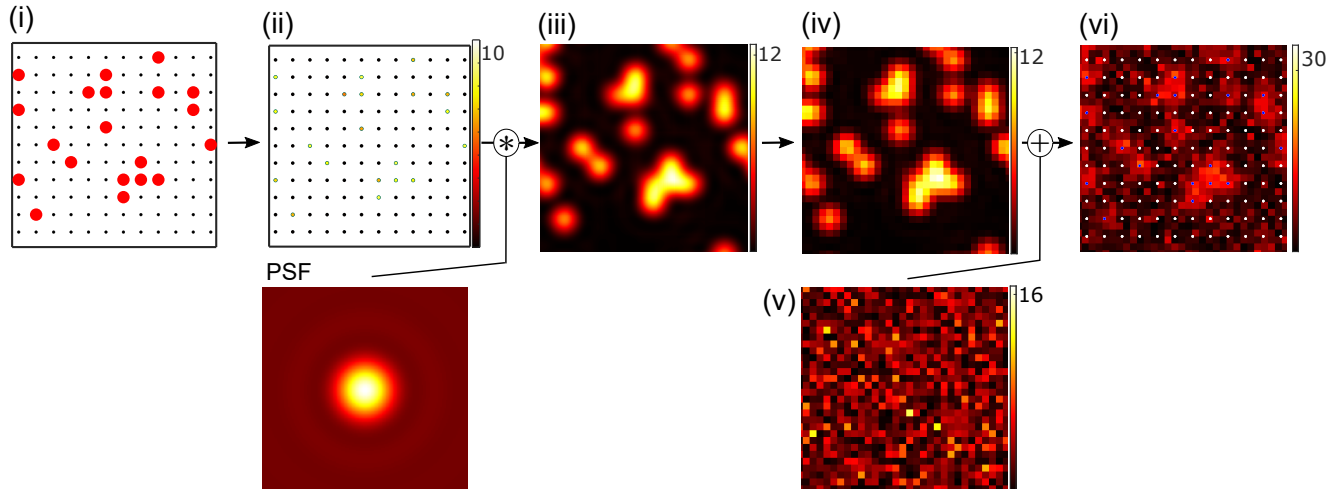


FIG. 1: Simulation of fluorescences imaging of ultracold atoms in an optical lattice. The numbered panels refer to the simulation steps in the text. (i) the atomic distribution, (ii) the signal per site in the image plane, (iii) the convolved signal after convolution with the normalised PSF shown below, (iv) the signal as recorded by the camera showing pixelation and (v) the generated background noise. The final simulated image (vi) is the sum of (iv) and (v) including the Poissonian EMCCD gain. Each panel shows a region of 12×12 lattice sites. The colorbars in panel (ii) and (iii) show the signal per atom and the colorbars in panels (iv)-(vi) show the signal per pixel ($\times 1000$).

Our goal is to identify the best deconvolution algorithm capable of reconstructing the known lattice occupation $n_{i,j}$ with the highest fidelity, first as a function of lattice occupation, η , and SNR only, then also including varying atomic fluorescence levels and resolution. While such a reconstruction is possible with high fidelity in the case of sparse filling, this will be increasingly difficult in the case of dense filling and low signal.

III. DECONVOLUTION TECHNIQUES

In this study, we use three different deconvolution methods, a 'local iterative' (LI) deconvolution algorithm, the Lucy-Richardson (LR) algorithm, and the Wiener deconvolution. Both Wiener and LR algorithms are widely used in microscopy applications ranging from biology to astronomy [30, 31]. The LI deconvolution algorithm was used in one of the first quantum-gas microscope experiments [3] to determine the lattice occupancy of Mott-insulator images with dense filling. All our simulation and deconvolution methods were implemented in Matlab [32, 33]. The algorithms use a discrete PSF as an input (I_{PSF}), which can be measured with a higher resolution than the microscope images by averaging multiple images of single atoms using sub-pixel scaling [26]. In our study, a PSF with a resolution five times higher than the imaging resolution is used. In the following, we provide a detailed description of each method.

The LI algorithm [3] finds the most likely distribution of atoms by placing point-spread functions of variable amplitudes on the known lattice grid, using an optimisation method similar to a fitting algorithm. It minimises the difference between the camera image and a reconstructed image, by trying different local permutations and by varying the amplitudes $A_{k,l}$. The algorithm optimises locally, in the vicinity of ± 10 sites around each lattice site, and then iteratively moves across all lattice sites. A typical image after LI deconvolution is shown in Fig. 3b for $\text{SNR} = 2$. A histogram of the optimised amplitudes $A_{k,l}$ shows two peaks, corresponding to empty and occupied lattice sites, as shown in Fig. 2c). We fit the distribution with bimodal Gaussian, and find a threshold value between the two peaks at the intersection of the two Gaussians. A lattice site with a signal amplitude above the threshold is considered occupied ($\tilde{n}_{k,l} = 1$). Finally, we calculate the reconstruction fidelity, F , as the fraction of correctly identified lattice site occupations,

$$F = 1 - \frac{1}{N^2} \sum_{k,l=1}^N |n_{k,l} - \tilde{n}_{k,l}|. \quad (4)$$

The second algorithm is the Wiener deconvolution [25], a method that employs an inverse Fourier filter weighted by a factor K that is proportional to the noise-to-signal ratio and includes the Fourier transform of both the camera

image I and the discretised PSF, I_{PSF} ,

$$W = \tilde{\mathcal{F}} \left[\frac{\mathcal{F}(I)}{\mathcal{F}(I_{\text{PSF}}) \frac{|\mathcal{F}(I_{\text{PSF}})|^2}{|\mathcal{F}(I_{\text{PSF}})|^2 + K}} \right], \quad (5)$$

where W is the deconvolved image, and $\mathcal{F}(\cdot)$ and $\tilde{\mathcal{F}}(\cdot)$ are the Fourier and inverse Fourier transforms, respectively. As K is a priori unknown, we developed a protocol to determine the optimum K value for a given image. The regular spacing of the atoms in the lattice leads to peaks in the fast Fourier transform of the deconvolved images, at a distance from the centre corresponding to the inverse lattice spacing [Fig. 2a)]. To find the optimum K for which these peaks are most prominent, we compare the peak heights for images deconvolved with different K [Fig. 2b)]. To reduce fringes occurring during the Fourier transforms, we blur the outer 30 pixels in each image [32]. After deconvolution with the optimal K value, the signal of each lattice site is integrated within a circle of radius $a/2$, yielding the signal amplitudes $A_{k,l}$. As for the LI deconvolution, the histograms of the $A_{k,l}$ show a bimodal distribution, corresponding to empty and occupied lattice sites [Fig. 2c)], and again a threshold value is found by a bimodal Gaussian fit. An example of a Wiener-deconvolved image is shown in Fig. 3d.

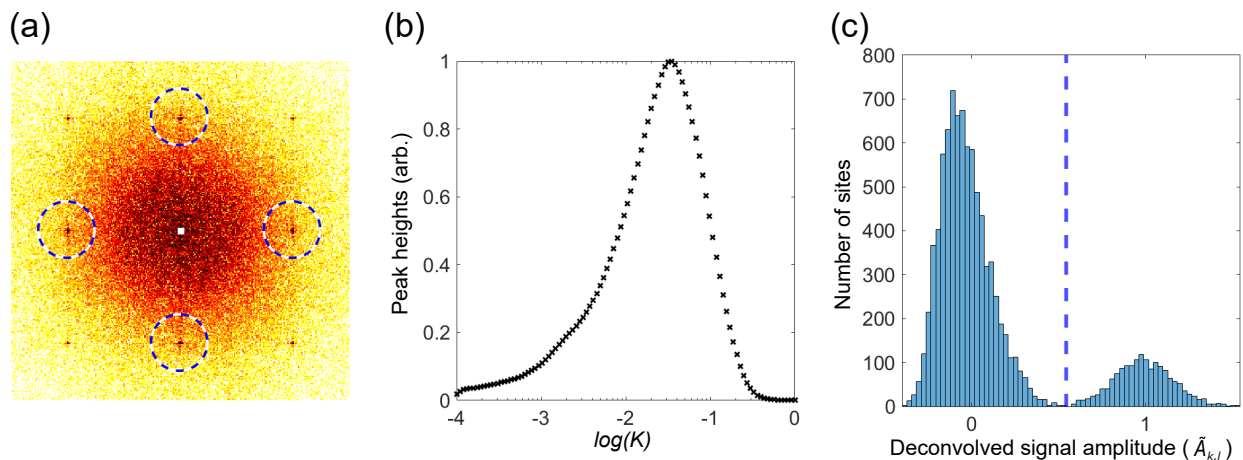


FIG. 2: Optimising the Wiener deconvolution protocol. a) FFT of an image after Wiener deconvolution with the optimal deconvolution parameter K . The four encircled peaks are the first-order harmonics at the inverse lattice spacing (the zeroth order in the center is removed to enhance the contrast). The dashed circles are a guide to the reader only. b) The signal at these four peaks as a function of K allows us to determine its optimal value. This plot is normalised. c) The histogram of deconvolved signal amplitude per site $\tilde{A}_{k,l}$ for using the optimum K found in b). The threshold above which sites are considered occupied is shown by the dashed line.

The Lucy-Richardson (LR) deconvolution is a Bayesian-based maximum-likelihood estimation, capable of calculating the most likely original image in the presence of noise and blurring due to convolution with a (known or unknown) point-spread function. We use the Matlab function `DECONVLUCY(I, I_{PSF}, m)`, with the input image I , the PSF, and the number of iterations m , which is a free parameter. We found that a fixed number of 7 iterations results in the best atom reconstruction fidelity for all parameters regimes discussed in Sections IVa-b. Similar to the Wiener deconvolution, we also blur the edges of the images. We also found that the fidelity is increased when we apply a low-pass Fourier filter to the original image because it reduces the effect of pixelation. The filter has a cutoff set by the spatial frequency of $1/(1.8d_{\text{min}})$. After deconvolution, the signal around each lattice site is integrated and the lattice occupation is calculated in the same way as for the Wiener method.

We tested each technique in combination with other filters, such as higher frequency low-pass filters, not filtering at all, and by using various weighting and masking options provided by MATLAB. The results below are generated by the methods described above and represent the most successful version of each deconvolution protocol. For the LI method, a simulated background image was subtracted to obtain an image without offset, and we use images with offset for the Wiener and LR methods. For all deconvolution methods, we upscaled the resolution of the simulated images by a factor of five in order to match the resolution of the PSF. We can alternatively downscale the PSF to match the image resolution, which greatly increases the computation speed, but it reduces the atom detection fidelity by at least several percent. We qualitatively compare the three deconvolution methods and the resulting estimated

occupation using a test image with $\text{SNR} = 2$ (Fig. 3). Such a low SNR makes it challenging to identify atoms by eye, and we can see how each method increases the image contrast in different ways. The LR algorithm reduces the noise in the image while the Wiener method creates a wavelike pattern with high maxima at occupied sites.

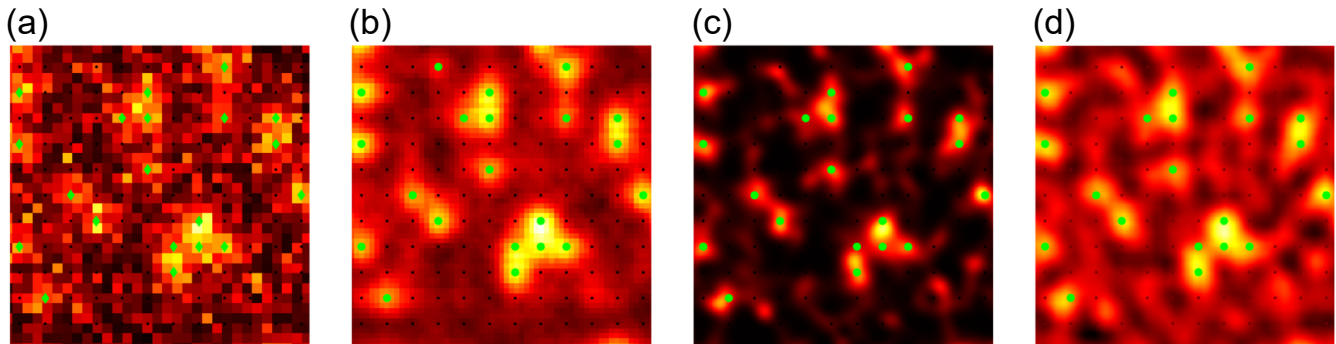


FIG. 3: Comparison of deconvolved images. a) Section of a simulated image with low signal-to-noise ratio ($\text{SNR} = 2$), generated using the protocol described in Section 2. Occupied sites are indicated by the green diamonds. b) Reconstructed image generated by the Local Iterative deconvolution algorithm. c) Deconvolved image created by the Lucy-Richardson algorithm, and d) by the Wiener method with optimised K parameter. The sites identified as occupied by each method are marked with green circles and empty sites as small black dots. All images are normalised to allow for better comparison.

IV. RESULTS

A. Comparing deconvolution methods

We first compare the reconstruction fidelity of the different deconvolution methods (Fig. 4) for varying lattice filling and signal-to-noise ratios, with the same simulated fluorescence signal for all atoms ($\Delta A = 0$). We find that the LR and Wiener methods have the highest reconstruction fidelity, with $F > 95\%$ for $\text{SNR} = 1$ and $F > 99\%$ for $\text{SNR} = 2$. In comparison, the LI method only achieves $F < 90\%$ for $\text{SNR} = 1$ for filling factors $\eta > 50\%$, and F decreases further with increasing η . Both Wiener and LR methods are least reliable around 50% filling, and require $\text{SNR} > 1.5$ to obtain an error rate of below 2%, and both achieve $F > 99.9\%$ for $\text{SNR} > 2.5$. The fidelity of the LI method is less good throughout for all parameters and most noticeably for higher filling and $\text{SNR} < 3$.

A key difference between the methods is the computation time required. On a standard desktop PC, the LI method requires up to two minutes to deconvolve an image and the computation time scales with the number of occupied sites. In contrast, the LR and Wiener methods (fixed K) require only several seconds per deconvolution, independent of η . The automated Wiener protocol can require up to one minute per image, as about 40 deconvolutions are needed to find the best K .

B. Including inhomogeneous fluorescence

In real quantum-gas microscope images, the amount of fluorescence light emitted varies from atom to atom, e.g., due to inhomogeneous cooling laser-light intensity or polarisation, or due to spatially varying trapping frequencies. Atoms also have a small but finite probability of being heated out of a lattice site and being re-trapped on a different site. These loss and hopping events can also reduce the amount of fluorescence light collected from an atom. While one could in principle simulate these processes individually, we choose to consider only the resulting effect of inhomogeneous fluorescence. For this purpose we simulated microscope images with a variation of $\pm 20\%$ and $\pm 40\%$ of the amplitudes $A_{i,j}$ around the mean value \bar{A} ($\Delta A/\bar{A} = 0.2$ and 0.4). We again use the three different deconvolution algorithms and compare the reconstruction fidelity (Fig. 5) after averaging over the five filling levels used previously. As expected, for all methods we see a drop in detection fidelity for increasing inhomogeneity. We also find that the Wiener and LR methods are less prone to inhomogeneous fluorescence ($F > 99.5\%$ for $\text{SNR} = 2.5$, $\Delta A/\bar{A} = 0.4$), compared to the LI algorithm for which we see a lower fidelity ($F < 97\%$) using the same parameters.

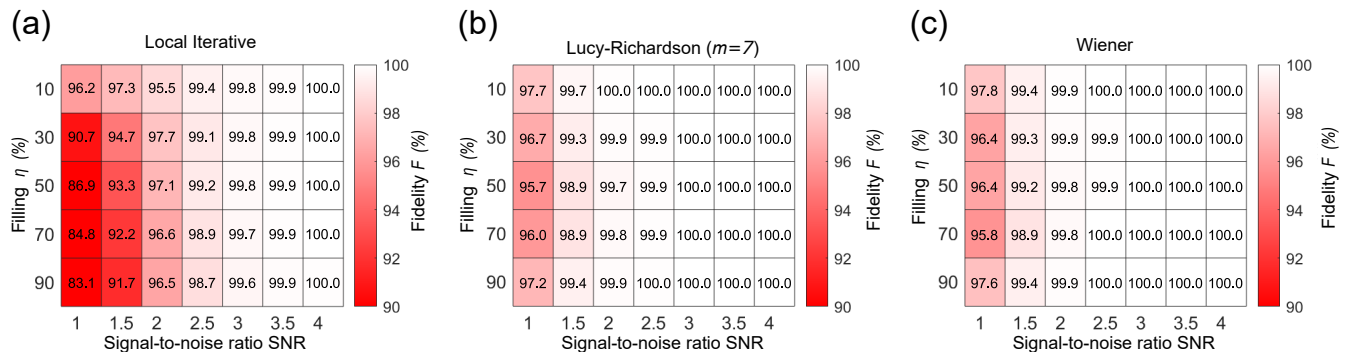


FIG. 4: Comparison of deconvolution methods. Reconstruction fidelity for simulated images with varying SNR and lattice filling fraction η , using a) the Local Iterative deconvolution, b) the Lucy-Richardson algorithm (7 iterations), c) the Wiener deconvolution with optimised K parameter.

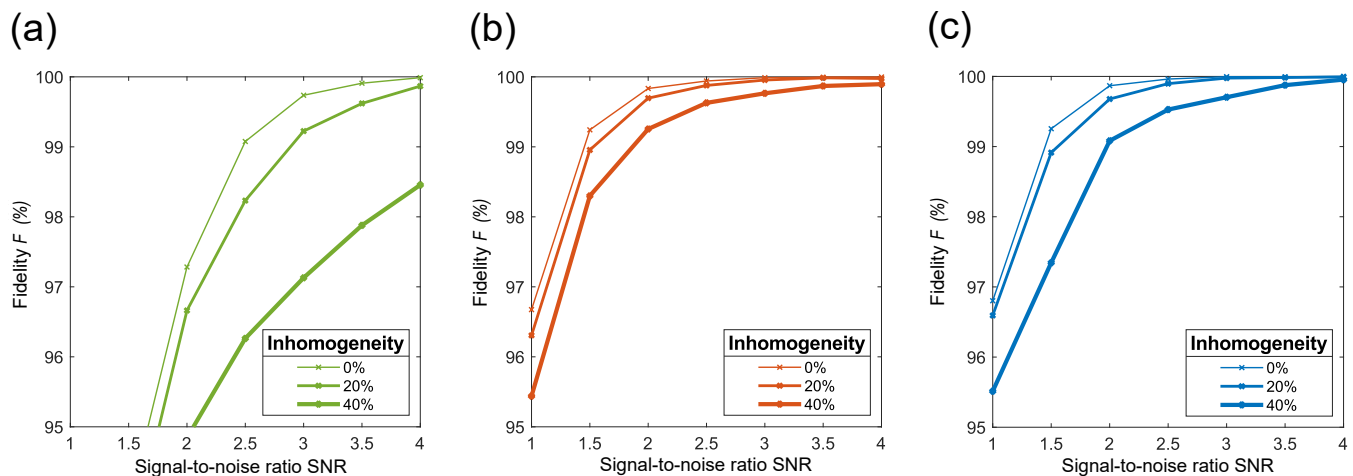


FIG. 5: Atom-detection fidelity in the presence of inhomogeneous fluorescence with $\frac{\Delta A}{A} = (0, \pm 20\%, \text{ and } \pm 40\%)$ after deconvolution using a) the Local Iterative method, b) the Lucy-Richardson algorithm and c) the Wiener algorithm. The results shown are an average over the five filling levels (10%, 30%, 50%, 70% and 90%) used in Fig 4.

C. Varying the resolution

We now consider the effect of the image magnification and pixelation on the reconstruction fidelity. In many quantum-gas microscope experiments, one lattice site imaged to about 4×4 pixels [3–7, 14–22]. Several groups have shown how sub-wavelength traps can be created for ultracold atoms [34–36], and in recent experiments, Erbium atoms were imaged in an optical lattice with a spacing $a_L = 266$ nm [20]. Single-atom detection in such systems is challenging and our simulations will help to understand how SNR and resolution affect the deconvolution methods. A microscope-imaging setup can be characterized by the objective’s numerical aperture, NA, the fluorescence wavelength, λ , and the lattice spacing, a . The magnification, M , and pixelation, p ($p = Ma/d_{\text{pix}}$), can be varied independently of this. In previous studies, the minimum number of pixels required to resolve atomic positions on a lattice without loss of information is reasoned to be $p = 2.5$ [27, 37], based on linear-optics calculations (Shannon-Nyquist sampling).

Here we investigate both the effect of changing the number of pixels per lattice site p and of operating near or below the diffraction limit. We generated simulated images where the lattice spacing is varied from $a = 200$ nm to $a = 1.2 \mu\text{m}$. This corresponds to varying the ratio of lattice spacing over diffraction limit, $\beta = a/d_{\text{min}}$, in the range $0.29 < \beta < 1.74$. We vary the pixelation in four steps from 2.5 to 4 pixels per lattice site while we keep the magnification fixed. The local-iterative deconvolution is no longer used here as it achieved consistently lower fidelities. We evaluate the reconstruction fidelity for $\text{SNR} = 2$ and $\text{SNR} = 4$, and we see a markedly reduced fidelity for atom

separations well below the Rayleigh limit for both deconvolution techniques (Fig. 6). Sparrow’s limit, defined as the distance between objects where the local minimum in between their overlapping point-spread functions vanishes, ($0.77 d_{min}$), and it matches the point at which perfect reconstruction becomes impossible. In Fig. 6, Rayleigh’s and Sparrow’s limits are shown by the dashed and dotted lines, respectively.

When comparing the results for $\text{SNR} = 2$ and $\text{SNR} = 4$, one finds that more pixels per lattice spacing can improve the fidelity, most notably when the signal is lower. The Nyquist sampling limit can be recognised in our results, because only for $p > 3.0$ we reach perfect reconstruction. We found that when the signal is equal to the background noise ($\text{SNR} = 1$) there is no observable scaling with the lattice spacing (or β) and increasing the pixelation cannot increase the fidelity beyond 95%. Both the LR and Wiener protocols show a reduced fidelity when the lattice spacing is increased beyond the resolution limit, and when the signal is low. The images in this regime have a pixelation noise that is higher than the fluorescence signal and background noise. We find that when the lattice spacing equals the diffraction limit, the protocol to optimise the Wiener K parameter gives $K = 1$, and $K > 1$ for larger lattice spacings. This confirms that in these images the noise is dominant. The highest fidelity is reached when one deconvolves with $K = 1$ for all lattice spacings that are larger than the diffraction limit as shown in Fig. 6. In this regime we find that for the Lucy-Richardson deconvolution a higher fidelity is reached when doing fewer iterations ($m = 3 - 5$). Both methods show a similar scaling of the fidelity with β for $\text{SNR} = 2$ and 4.

V. CONCLUSION

We have studied the detection fidelity of three different deconvolution techniques on simulated quantum-gas microscope images. The fidelity of each method scales differently with SNR level and lattice filling. The LR method was found to be the best which yielded the highest reconstruction fidelities. The LI method was found to be least efficient for high-filling ($\eta > 50\%$) and required most computation time. The LR method was least affected by inhomogeneities in the atom brightness. Both the LR and Wiener deconvolution were able to accurately identify atoms on lattice sites separated by 0.5 times the diffraction limit, provided that the pixelation is above the Nyquist sampling threshold and that the images have a good signal-to-noise ($\text{SNR} > 4.0$). It was shown how the reconstruction fidelities are affected when pixelation noise becomes dominant. Our methods are scalable and applicable to a wide-range of quantum-gas microscope images with different resolution, wavelengths and lattice spacing. In future studies atom hopping and loss events that occasionally occur during imaging could also be incorporated in the simulation [26, 38], as well as possible sub- and super-radiance effects [39–41], which cause a density-dependent fluorescence per atom.

VI. ACKNOWLEDGMENTS

We acknowledge support by the EPSRC through the Programme Grant DesOEQ (EP/P009565/1), the Quantum Technology Hub in Quantum Computing and Simulation (EP/T001062/1) and the New Investigator Grant (EP/T027789/1).

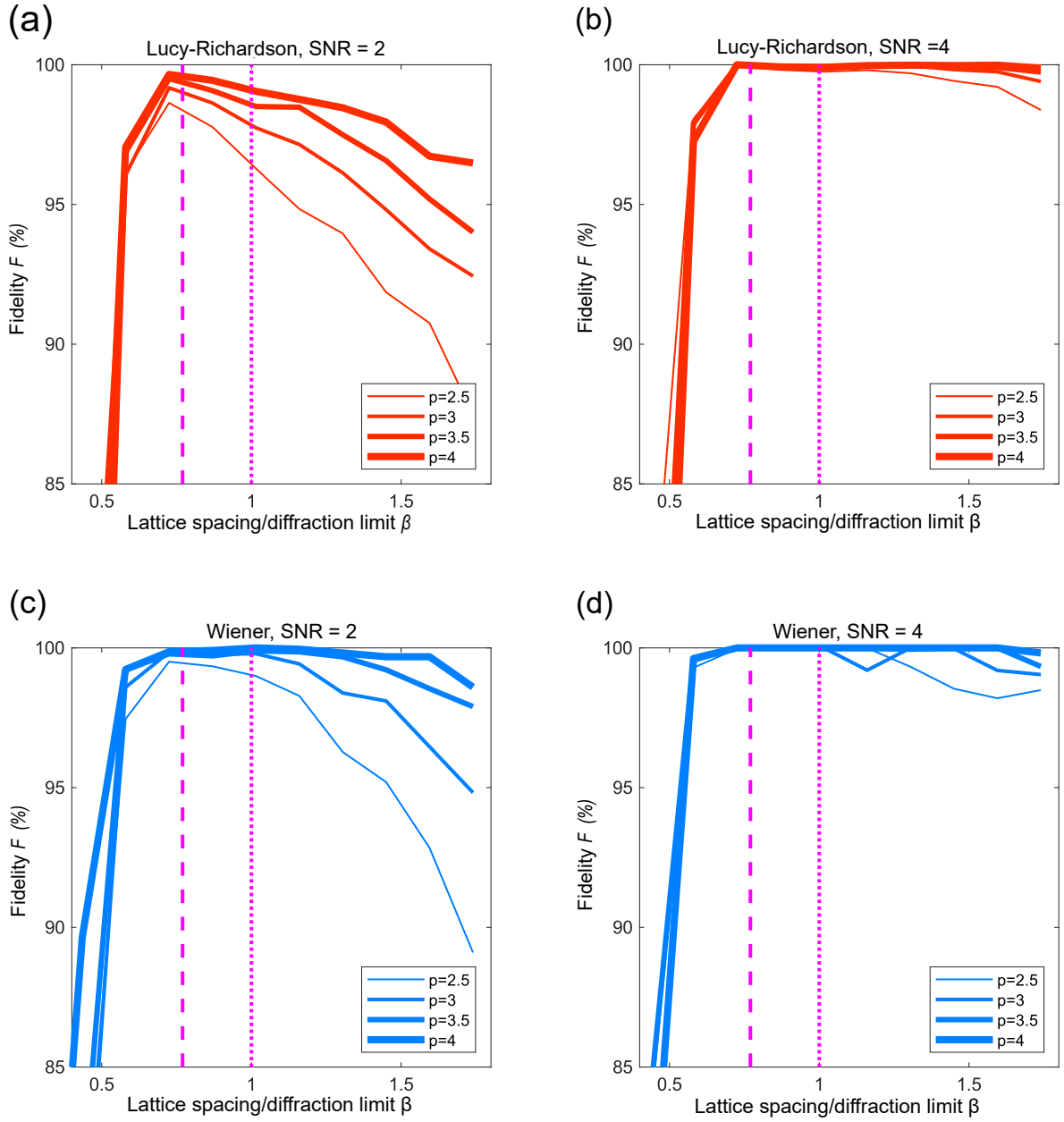


FIG. 6: Reconstruction fidelity of simulated images with 50% filling, for varying resolution parameters $\beta = a/d_{min}$, and pixelation $p = 2.5, 3, 3.5$ and 4. a) and b) The fidelity for the LR algorithm for images with SNR = 2 and SNR = 4. seven Lucy-Richardson iterations are used for all deconvolutions. c) and d) The fidelity for the Wiener algorithm with SNR = 2 and SNR = 4. Here the Wiener protocol with optimised K is used for $\beta < 1$ and when $\beta > 1$ K is set to 1. Each point is an average fidelity from five simulated images. The Rayleigh and Sparrow diffraction limits are shown as dotted and dashed vertical lines respectively.

VII. REFERENCES

-
- [1] W. S. Bakr, J. I. Gillen, A. Peng, S. Fölling, and M. Greiner, A quantum gas microscope for detecting single atoms in a hubbard-regime optical lattice, *Nature* **462**, 74 (2009).
- [2] I. Bloch, J. Dalibard, and W. Zwerger, Many-body physics with ultracold gases, *Rev. Mod. Phys.* **80**, 885 (2008).
- [3] J. F. Sherson, C. Weitenberg, M. Endres, M. Cheneau, I. Bloch, and S. Kuhr, Single-atom-resolved fluorescence imaging of an atomic mott insulator, *Nature* **467**, 68 (2010).
- [4] W. S. Bakr, A. Peng, M. E. Tai, R. Ma, J. Simon, J. I. Gillen, S. Foelling, L. Pollet, and M. Greiner, Probing the superfluid-to-mott insulator transition at the single-atom level, *Science* **329**, 547 (2010).
- [5] L. W. Cheuk, M. A. Nichols, M. Okan, T. Gersdorf, V. V. Ramasesh, W. S. Bakr, T. Lompe, and M. W. Zwierlein, Quantum-gas microscope for fermionic atoms, *Phys. Rev. Lett.* **114**, 193001 (2015).
- [6] D. Greif, M. F. Parsons, A. Mazurenko, C. S. Chiu, S. Blatt, F. Huber, G. Ji, and M. Greiner, Site-resolved imaging of a fermionic mott insulator, *Science* **351**, 953 (2016).
- [7] G. J. Edge, R. Anderson, D. Jervis, D. C. McKay, R. Day, S. Trotzky, and J. H. Thywissen, Imaging and addressing of individual fermionic atoms in an optical lattice, *Phys. Rev. A* **92**, 063406 (2015).
- [8] M. Boll, T. A. Hilker, G. Salomon, A. Omran, J. Nespolo, L. Pollet, I. Bloch, and C. Gross, Spin- and density-resolved microscopy of antiferromagnetic correlations in fermi-hubbard chains, *Science* **353**, 1257 (2016).
- [9] A. Mazurenko, C. S. Chiu, G. Ji, M. F. Parsons, M. Kanász-Nagy, R. Schmidt, F. Grusdt, E. Demler, D. Greif, and M. Greiner, A cold-atom fermi-hubbard antiferromagnet, *Nature* **545**, 462 (2017).
- [10] J. Simon, W. S. Bakr, R. Ma, M. E. Tai, P. M. Preiss, and M. Greiner, Quantum simulation of antiferromagnetic spin chains in an optical lattice, *Nature* **472**, 307 (2011).
- [11] T. Fukuhara, A. Kantian, M. Endres, M. Cheneau, P. Schauß, S. Hild, D. Bellem, U. Schollwöck, T. Giamarchi, C. Gross, *et al.*, Quantum dynamics of a mobile spin impurity, *Nature Phys* **9**, 235 (2013).
- [12] P. M. Preiss, R. Ma, M. E. Tai, A. Lukin, M. Rispoli, P. Zupancic, Y. Lahini, R. Islam, and M. Greiner, Strongly correlated quantum walks in optical lattices, *Science* **347**, 1229 (2015).
- [13] A. Bohrdt, C. S. Chiu, G. Ji, M. Xu, D. Greif, M. Greiner, E. Demler, F. Grusdt, and M. Knap, Classifying snapshots of the doped hubbard model with machine learning, *Nat. Phys.* **15**, 921 (2019).
- [14] R. Yamamoto, H. Ozawa, D. C. Nak, I. Nakamura, and T. Fukuhara, Single-site-resolved imaging of ultracold atoms in a triangular optical lattice, *New J. Phys.* **22**, 123028 (2020).
- [15] L. Liu, J. Mongkolkiattichai, J. Yang, and P. Schauss, Site-resolved imaging of ultracold fermions in triangular-lattice quantum gas microscope, *PRX Quantum* **2**, 020344 (2021).
- [16] L. Asteria, H. P. Zahn, M. N. Kosch, K. Sengstock, and C. Weitenberg, Quantum gas magnifier for sub-lattice-resolved imaging of 3d quantum systems, *Nature* **599**, 571 (2021).
- [17] K. D. Nelson, X. Li, and D. S. Weiss, Imaging single atoms in a three-dimensional array, *Nature Phys* **3**, 556 (2007).
- [18] A. J. Krahn, *Erbium Quantum Gas Microscope*, Ph.D. thesis, Harvard University (2021).
- [19] I. Knottnerus, S. Pyatchenkov, O. Onishchenko, A. Urech, F. Schreck, and G. Siviloglou, Microscope objective for imaging atomic strontium with 0.63 micrometer resolution, *Opt. Express* **28**, 11106 (2020).
- [20] L. R. Picard, M. J. Mark, F. Ferlaino, and R. van Bijnen, Deep learning-assisted classification of site-resolved quantum gas microscope images, *Meas. Sci. Technol.* **31**, 025201 (2019).
- [21] R. Yamamoto, J. Kobayashi, T. Kuno, K. Kato, and Y. Takahashi, An ytterbium quantum gas microscope with narrow-line laser cooling, *New J. Phys.* **18**, 023016 (2016).
- [22] G. A. Phelps, *A dipolar quantum gas microscope*, Ph.D. thesis, Massachusetts Institute of Technology (2019).
- [23] L. B. Lucy, An iterative technique for the rectification of observed distributions, *Astronomical Journal* **79**, 745 (1974).
- [24] W. H. Richardson, Bayesian-based iterative method of image restoration, *JoSA* **62**, 55 (1972).
- [25] N. Wiener, *Extrapolation, Interpolation, and Smoothing of Stationary Time Series: With Engineering Applications*, Vol. 8 (MIT Press, 1964).
- [26] E. Haller, J. Hudson, A. Kelly, D. A. Cotta, B. Peaudecerf, G. D. Bruce, and S. Kuhr, Single-atom imaging of fermions in a quantum-gas microscope, *Nature Phys* **11**, 738 (2015).
- [27] A. Alberti, C. Robens, W. Alt, S. Brakhane, M. Karski, R. Reimann, A. Widera, and D. Meschede, Super-resolution microscopy of single atoms in optical lattices, *New J. Phys.* **18**, 053010 (2016).
- [28] ANDOR iXon Ultra 897, (andor.oxinst.com/assets/uploads/products/andor/documents/andor-ixon-ultra-emccd-specifications.pdf).
- [29] Poissonian filter in matlab.
- [30] R. Manwar, M. Zafar, and Q. Xu, Signal and image processing in biomedical photoacoustic imaging: A review, *Optics* **2**, 1 (2021).
- [31] J.-L. Starck, E. Pantin, and F. Murtagh, Deconvolution in astronomy: A review, *PASP* **114**, 1051 (2002).
- [32] Wiener deconvolution in Matlab.
- [33] Lucy Richardson deconvolution in Matlab.

- [34] A. La Rooij, S. Couet, M. Van Der Krogt, A. Vantomme, K. Temst, and R. Spreeuw, Deposition and patterning of magnetic atom trap lattices in fept films with periods down to 200nm, *Journal of Applied Physics* **124**, 044902 (2018).
- [35] A. González-Tudela, C.-L. Hung, D. E. Chang, J. I. Cirac, and H. Kimble, Subwavelength vacuum lattices and atom–atom interactions in two-dimensional photonic crystals, *Nature Photon* **9**, 320 (2015).
- [36] Y. Wang, S. Subhankar, P. Bienias, M. Łącki, T.-C. Tsui, M. A. Baranov, A. V. Gorshkov, P. Zoller, J. V. Porto, and S. L. Rolston, Dark state optical lattice with a subwavelength spatial structure, *Phys. Rev. Lett.* **120**, 083601 (2018).
- [37] J. B. Pawley, Points, pixels, and gray levels: Digitizing image data, in *Handbook of Biological Confocal Microscopy* (Springer, 2006) pp. 59–79.
- [38] T. A. Hilker, *Spin-resolved microscopy of strongly correlated fermionic many-body states*, Ph.D. thesis, Ludwig Maximilians Universität München (2017).
- [39] G. Facchinetti, S. D. Jenkins, and J. Ruostekoski, Storing light with subradiant correlations in arrays of atoms, *Phys. Rev. Lett.* **117**, 243601 (2016).
- [40] G. Facchinetti and J. Ruostekoski, Interaction of light with planar lattices of atoms: Reflection, transmission, and cooperative magnetometry, *Phys. Rev. A* **97**, 023833 (2018).
- [41] J. Rui, D. Wei, A. Rubio-Abadal, S. Hollerith, J. Zeiher, D. M. Stamper-Kurn, C. Gross, and I. Bloch, A subradiant optical mirror formed by a single structured atomic layer, *Nature* **583**, 369 (2020).